AIAA JOURNAL
Vol. 37, No. 7, July 1999

Reynolds-Stress-Transport Modeling for Compressible Aerodynamics Applications

P. Batten,* T. J. Craft,† M. A. Leschziner,‡ and H. Loyau*
UMIST, Manchester, England M60 1QD, United Kingdom

Progress is reported in the development of a nonlinear Reynolds-stress-transport model for compressible, turbulent flow. The focus is on a variation of a particular cubic model that does not require the usual topography-related parameters, such as normal-to-wall vectors. However, certain wall-proximity corrections that have been used in the model to replace conventional wall-reflection terms display the wrong response to shocks, which are falsely interpreted as localized regions of strong inhomogeneity. A modified cubic variant is proposed that allows integration across the semiviscous sublayer and incorporates additional constraints to guard against unphysical response of the pressure–strain model in the vicinity of shock waves. The modified model is applied to both two- and three-dimensional compressible flows, involving shock-wave/boundary-layer interaction, and is shown to yield generally favorable results.

Nomenclature

A	= Lumley's stress-flatness parameter, $1 - 9/8(A_2 - A_3)$
A_2	= second invariant of stress-anisotropy tensor, $a_{ij}a_{ij}$
A_3	= third invariant of stress-anisotropy tensor, $a_{ij}a_{jk}a_{ki}$
a_{ij}	= dimensionless stress-anisotropy tensor $\widetilde{u_i''u_j''}/\tilde{k} - 2\delta_{ij}/3$
d_i, d_i^A	= normalized direction-indicator vectors
d_{ij}	= diffusive transport of $\widetilde{u_i''u_j''}$
d_{ij}^p	= diffusive transport of $\widetilde{u_i''u_j''}$ due to pressure fluctuations
$\tilde{k}$	= mass-averaged turbulent kinetic energy
l, l_e	= turbulence length scale and equilibrium length scale
N_i, N_i^A	= length-scale and modified length-scale-gradient vectors
P_{ij}	= stress-production tensor
Re_t	= turbulent Reynolds number, $\tilde{k}^2/\tilde{\nu}\tilde{\epsilon}$
$\widetilde{u_i''u_j''}$	= Reynolds-averaged Reynolds-stress tensor
x_j	= Cartesian coordinate vector
δ_{ij}	= Kronecker delta
ϵ_{ij}	= dissipation rate of $\widetilde{u_i''u_j''}$
$\tilde{\epsilon}$	= dissipation rate of $\tilde{k}$, $\tilde{\epsilon}^* + 2\tilde{\nu}(\partial\tilde{k}^{1/2}/\partial x_j)^2$
$\tilde{\epsilon}^*$	= homogeneous dissipation rate of $\tilde{k}$
χ_{ij}^*	= modified pressure–strain tensor
χ_{ij1}^*, χ_{ij2}^*	= turbulent and mean-strain contributions to χ_{ij}^*

I. Introduction

ALTHOUGH much progress has been made over the past two decades in second-moment modeling of turbulent flow, simpler eddy-viscosity models continue to enjoy undiminished popularity in practice. This is especially so in the area of compressible flow, where turbulence is often viewed as a second-order process, relative to pressure and advection. Even in circumstances in which turbulence is highly influential, e.g., shock/boundary-layer interaction, the desire for simplicity and economy tends to outweigh arguments for generality and physical realism, and highly tuned eddy-viscosity models remain the preferred option.

A factor that favors eddy-viscosity models in many high-speed-flow applications is that influential turbulent processes tend to be confined to relatively thin near-wall regions. This is so even in the case of shock-induced separation, where the recirculation zone is usually thin and highly elongated. In the case of two-dimensional flow, the primary requirement is then for the correct prediction of the single dynamically active shear stress. This explains the success and popularity of well-tuned eddy-viscosity models, such as Menter's shear-stress-transport model[1] and Spalart and Allmaras's[2] one-equation turbulent-viscosity model. Although a realistic resolution of the normal stresses is not essential in the described circumstances, it usually is important in the presence of massive separation and three-dimensional flows containing streamwise vorticity and high streamline curvature, e.g., swirl. Moreover, interest may extend beyond the prediction of gross aerodynamic features, such as the size of the primary separated zone provoked by a shock, and in this case, a more refined representation of the turbulence structure may be critical to success.

Apart from the obvious increase in complexity, numerical brittleness, and resource requirements, the restriction of most existing Reynolds-stress models to nearly incompressible flow (at least in the design and calibration stage) has been a major factor discouraging their adoption. Experience suggests that models designed and tested exclusively in incompressible flows may give poor or even disastrously wrong predictions in flows involving shock-wave/boundary-layer interaction. One such example is the Launder–Shima model[3] and variants thereof,[4,5] which contain terms sensitized to the ratio of turbulence production to dissipation rate (P_k/ϵ), a nonequilibrium indicator in the $C_{\epsilon 1}$ coefficient of the dissipation equation. This sensitization appears to work well in incompressible flow with mild adverse pressure gradient,[3–5] but has been found to return an excessive response in shock-affected flow, giving too much damping of the turbulence energy, to the extent of provoking nonphysical relaminarization downstream of shock waves (see, e.g., Ref. 6).

Reynolds-stress models incorporating linear pressure–strain approximations, e.g., those of Launder et al.[7] and of Gibson and Launder,[8] have been used successfully for many years in modeling incompressible turbulent flows involving substantial streamline curvature, swirl, separation, and density stratification, where they usually outperform eddy-viscosity formulations. These models have also been reported to return superior predictive performance for strong shock/boundary-layer interaction in transonic flows.[9–12] However, they require a supplementary near-wall model of lower order to bridge the semiviscous near-wall layer, and, more importantly, they rely on highly influential wall-specific corrections designed to return the preferential damping of normal-to-wall fluctuations, consistent with the approach of turbulence to the two-component limit at a wall. These corrections typically require knowledge of the local surface topography, as they involve the local wall-normal distance and normal-to-wall vector. Because the normal-to-wall vector has no unique definition in the vicinity of complex geometrical features,

Received 13 August 1998; revision received 20 January 1999; accepted for publication 2 February 1999.

*Research Associate, Department of Mechanical Engineering.
†Research Fellow, Department of Mechanical Engineering.
‡Professor of Computational Fluid Dynamics, Department of Mechanical Engineering, P.O. Box 88; M.Leschziner@umist.ac.uk. Member AIAA.

recent work at UMIST, e.g., of Launder and Li,[13] has focused on the design of low-Reynolds-number closures that do not require such parameters and, indeed, represent adequately the near-wall state with much weaker explicit wall-proximity terms, owing to their use of nonlinear pressure–strain approximations. A similar strategy has been adopted by Speziale et al.,[14] whose model, although applicable to high Reynolds numbers only, is claimed to require no pressure–strain-related wall corrections at all.

The present modeling framework has its roots in the realizable Reynolds-stress closure of Fu,[15] which incorporates a tensorially cubic pressure–strain model. This model was developed and extended to low-Reynolds-number near-wall flows by Launder and Tselepidakis,[16] Launder and Li,[13] Craft and Launder,[17] and Craft.[18] All but two of the coefficients in Fu's[15] rapid pressure–strain model have been determined by imposing constraints such as symmetry, tensorial consistency, zero trace, and satisfaction of the two-component limit. Experience over the past decade at UMIST suggests that this model, although undeniably more elaborate than the early linear variants, offers improved predictive characteristics in a variety of complex strain fields. All of the recent low-Reynolds-number extensions of this model[13,16–18] have used inhomogeneity corrections determined without reference to geometry-dependent quantities, to ensure the appropriate wall-limiting behavior of the individual stresses.

Launder and Tselepidakis[16] originally introduced gradients of the turbulence length scale, $k^{3/2}/\epsilon$, to identify both regions and directions of strong inhomogeneity. Craft and Launder[17] refined this idea by incorporating the normalized, modified length-scale gradient

$$d_i^A = \frac{N_i^A}{\frac{1}{2} + \left(N_k^A N_k^A\right)^{\frac{1}{2}}}, \qquad N_i^A = \frac{\partial\left(k^{\frac{3}{2}} A^{\frac{1}{2}}/\epsilon\right)}{\partial x_i} \tag{1}$$

where A is Lumley's stress-flatness parameter, which varies between unity in isotropic turbulence and zero as the turbulence approaches a two-component limit. The modified length scale in Eq. (1) avoids the local minimum that the usual length scale, $l = k^{3/2}/\epsilon$, exhibits in the buffer region of the boundary layer. Craft[18] has further refined this cubic model by functionalizing the two free coefficients in the cubic pressure–strain model, by accounting for inhomogeneity effects associated with mean-velocity gradients and by approximating diffusive stress transport via an algebraic simplification of the triple-moment-transport equations. Good predictions are reported by Craft and Launder[17] and Craft[18] for a range of incompressible flows, including flows with separation and reattachment.

Unfortunately, the favorable performance of Craft and Launder's model in incompressible conditions does not carry over to compressible flows involving shocks. Figure 1 shows wall-pressure distributions computed for shock-induced separation over a channel bump[19] (see also Sec. IV.D). The predictions of the Craft–Launder[17] model are evidently worse than that of the widely used k–ϵ model of Launder and Sharma.[20] Not only does the former give a poor representation of the mean flow, but it also returns zero spanwise normal stress and vanishing stress-flatness parameter everywhere downstream of the shock. This misrepresentation is rooted in a combination of the dissipation equation being sensitized to the stress-flatness parameter and inhomogeneity corrections to the pressure–strain, which turn out to be inappropriately sensitive to the shock wave. In effect, the shock wave presents itself to the model as a steep localized gradient of the turbulence length scale, to which the inhomogeneity corrections to the pressure strain process respond by damping the normal fluctuations, as if the shock were a wall or free surface. However, in direct contradiction, direct numerical simulation (DNS) results by Mahesh et al.[21] indicate that the streamwise fluctuations are amplified through a normal shock wave. This can also be inferred from the exact stress-production terms. The nonphysical effect of these inhomogeneity corrections in the shock region is occasionally sufficient to cause the flatness parameter to tend toward zero downstream of the shock, indicating a two-component-limit state of turbulence. Because the model enforces a no-return to isotropy in this two-component limit, the predicted solutions do not recover downstream. In the two-dimensional example of the Délery case C (Fig. 1), this inhibits the transfer of turbulence energy into the spanwise normal stress. As this has no associated production term, it necessarily remains zero.

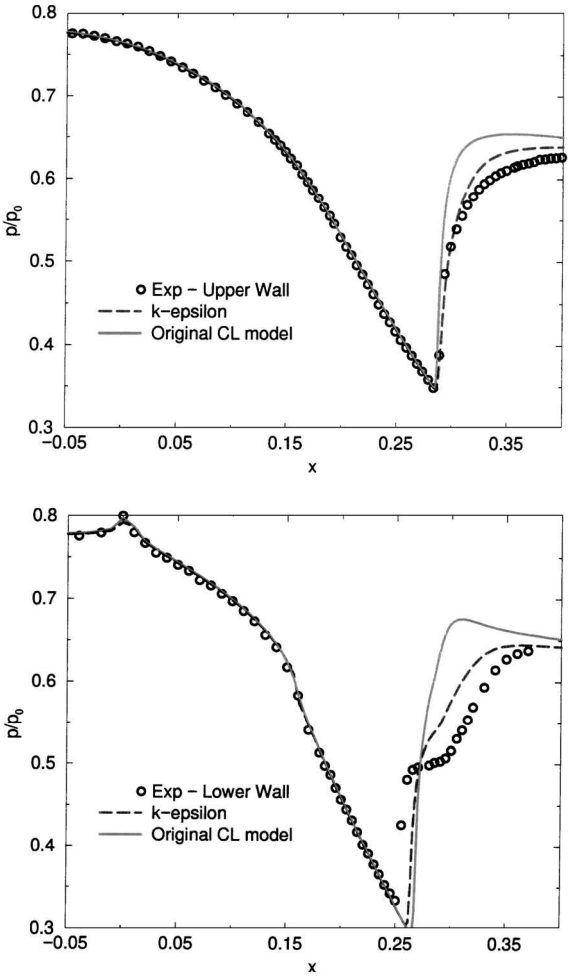

Fig. 1 Délery's case C: wall-pressure distributions.

The purpose of this paper is to present a variant of the recent Craft[18]/Craft–Launder[17] models, which has been designed and tested with reference to both incompressible and compressible flows. Additional constraints are included to avoid the earlier-mentioned excessive response of the pressure–strain model in the vicinity of shock waves, and simplifications are proposed for the dissipation-rate equation, triple moments, and turbulent heat fluxes.

II. Modified Cubic Reynolds-Stress Model

A. Model Foundation

With effects of density fluctuations ignored, the mass-averaged Reynolds-stress-transport equations may be written, in generic form, as follows:

$$\frac{\partial \bar{\rho}\,\widetilde{u_i'' u_j''}}{\partial t} + \frac{\partial \bar{\rho}\,\widetilde{u_i'' u_j''}\tilde{u}_k}{\partial x_k} = P_{ij} + d_{ij} + \chi_{ij}^* - \epsilon_{ij} \tag{2}$$

The closure approximations of the terms d_{ij}, χ_{ij}^*, and ϵ_{ij} are discussed in respective subsections to follow, with reference to corresponding approximations in Craft and Launder's[17] model for incompressible flows. In view of doubts cast on recent compressibility modifications for wall-bounded flows,[22] no such modifications have been implemented in the current version of the model.

B. Turbulent Diffusion: d_{ij}

The original form of the turbulence–diffusion model employed by Craft and Launder[17] was the 1972 Hanjalić–Launder proposal.[23] This is, essentially, one-half of the exact triple-moment production terms and has been argued to be more tensorially consistent than the simpler Generalized Gradient Diffusion Hypothesis (GGDH) and

more accurate in the near-wall region. However, Craft[18] points out that, toward the edge of the boundary layer, the Hanjalić–Launder[23] model predicts significantly more diffusion of $\widetilde{v''v''}$ than $\widetilde{w''w''}$. This was the cause for some difficulties in plane-channel and sudden-expansion flows and prompted Craft[18] to propose an algebraic triple-moment model in which all exact production terms are retained, along with additional models for diffusion, dissipation, and pressure correlation. Although this certainly represents a more general modeling route, it is not clear that such an algebraic model can be implemented in a stable fashion without the storage of all triple moments. For this reason, the simpler GGDH has been retained here:

$$d_{ij} = \frac{\partial}{\partial x_k}\left(\tilde{\mu}\frac{\partial \widetilde{u_i''u_j''}}{\partial x_k} + 0.22\frac{\bar{\rho}\tilde{k}}{\tilde{\epsilon}}\left[\widetilde{u_k''u_l''}\frac{\partial \widetilde{u_i''u_j''}}{\partial x_l}\right]\right) + \frac{d_{kk}^p\bar{\rho}\,\widetilde{u_i''u_j''}}{2\tilde{k}} \quad (3)$$

In Eq. (3), the last fragment represents pressure diffusion, and the present model form is a slight modification of that of Craft and Launder,[17] namely,

$$d_{kk}^p = -\frac{1}{\bar{\rho}}\left(\frac{\partial \overline{pu}_k}{\partial x_k}\right) \quad (4)$$

with

$$\overline{pu}_k = -\bar{\rho}(1-A)\left(0.5d_k + 1.1d_k^A\right)(\tilde{\nu}\tilde{\epsilon}\tilde{k}AA_2)^{\frac{1}{2}}C_{pd}$$
$$C_{pd} = [1 + 2\exp(-Re_t/40)]A_2 + 0.4Re_t^{-\frac{1}{4}}\exp(-Re_t/40) \quad (5)$$

In the preceding equations, the gradient-indicator vectors are

$$d_i = \frac{N_i}{[0.5 + \sqrt{N_k N_k}]}, \qquad d_i^A = \frac{N_i^A}{\left[0.5 + \sqrt{N_k^A N_k^A}\right]}$$

with

$$N_i = \frac{\partial(lA)}{\partial x_i}, \qquad N_i^A = \frac{\partial(l\sqrt{A})}{\partial x_i}, \qquad l = \frac{\tilde{k}^{\frac{3}{2}}}{\tilde{\epsilon}}$$

C. Pressure Correlation: ϕ_{ij}^*

The cubic pressure–strain model of Fu[15] is used in conjunction with coefficients and inhomogeneity corrections slightly modified from those proposed by Craft and Launder[17]:

$$\chi_{ij}^* = \chi_{ij1}^* + \chi_{ij2}^* + \chi_{ij1}^{\text{inh}} + \chi_{ij2}^{\text{inh}} \quad (6)$$

with

$$\chi_{ij1}^* = -c_1\bar{\rho}\tilde{\epsilon}^*\left[a_{ij} + c_1'\left(a_{ik}a_{kj} - \frac{1}{3}A_2\delta_{ij}\right)\right] - \bar{\rho}\tilde{\epsilon}^*A^{\frac{1}{2}}a_{ij}$$

$$\chi_{ij2}^* = -0.6\left(P_{ij} - \frac{1}{3}\delta_{ij}P_{kk}\right) + 0.3a_{ij}P_{kk}$$
$$- \frac{0.2\bar{\rho}}{\tilde{k}}\left[\widetilde{u_k''u_j''}\,\widetilde{u_l''u_i''}\left(\frac{\partial\tilde{u}_k}{\partial x_l} + \frac{\partial\tilde{u}_l}{\partial x_k}\right) - \widetilde{u_l''u_k''}\right.$$
$$\left.\times\left(\widetilde{u_i''u_k''}\frac{\partial\tilde{u}_j}{\partial x_l} + \widetilde{u_j''u_k''}\frac{\partial\tilde{u}_i}{\partial x_l}\right)\right] - c_2[A_2(P_{ij} - D_{ij}) + 3a_{mi}a_{nj}$$
$$\times(P_{mn} - D_{mn})] + c_2'\left\{\left(\frac{7}{15} - \frac{A_2}{4}\right)\left(P_{ij} - \frac{1}{3}\delta_{ij}P_{kk}\right)\right\}$$
$$+ 0.1\left[a_{ij} - \frac{1}{2}\left(a_{ik}a_{kj} - \frac{1}{3}\delta_{ij}A_2\right)\right]P_{kk} - 0.05a_{ij}a_{lk}P_{kl}$$
$$+ \frac{0.1}{\tilde{k}}\left[\left(\widetilde{u_i''u_m''}P_{mj} + \widetilde{u_j''u_m''}P_{mi}\right) - \frac{2}{3}\delta_{ij}\,\widetilde{u_l''u_m''}P_{ml}\right]$$
$$+ \frac{0.1}{\tilde{k}^2}\left[\widetilde{u_l''u_i''}\,\widetilde{u_k''u_j''} - \frac{1}{3}\delta_{ij}\,\widetilde{u_l''u_m''}\,\widetilde{u_k''u_m''}\right]$$
$$\times\left[6D_{lk} + 13\bar{\rho}\tilde{k}\left(\frac{\partial\tilde{u}_l}{\partial x_k} + \frac{\partial\tilde{u}_k}{\partial x_l}\right)\right] + \frac{0.2}{\tilde{k}^2}\,\widetilde{u_l''u_i''}\,\widetilde{u_k''u_j''}(D_{lk} - P_{lk})\Bigg\}$$

$$\chi_{ij1}^{\text{inh}} = f_{w1}\frac{\bar{\rho}\tilde{\epsilon}}{\tilde{k}}\left(\widetilde{u_l''u_k''}d_l^Ad_k^A\delta_{ij} - \frac{3}{2}\widetilde{u_i''u_k''}d_j^Ad_k^A - \frac{3}{2}\widetilde{u_j''u_k''}d_i^Ad_k^A\right)$$
$$+ f_{w2}\frac{\bar{\rho}\tilde{\epsilon}}{\tilde{k}^2}\left(\widetilde{u_m''u_n''}\,\widetilde{u_m''u_l''}d_n^Ad_l^A\delta_{ij} - \frac{3}{2}\widetilde{u_i''u_m''}\,\widetilde{u_m''u_l''}d_j^Ad_l^A\right.$$
$$\left. - \frac{3}{2}\widetilde{u_j''u_m''}\,\widetilde{u_m''u_l''}d_i^Ad_l^A\right)$$

$$\chi_{ij2}^{\text{inh}} = f_I\bar{\rho}\tilde{k}\frac{\partial u_l}{\partial x_n}d_ld_n\left(d_id_j - \frac{1}{3}d_kd_k\delta_{ij}\right)$$

with

$$P_{ij} = -\left(\bar{\rho}\,\widetilde{u_i''u_k''}\frac{\partial\tilde{u}_j}{\partial x_k} + \bar{\rho}\,\widetilde{u_j''u_k''}\frac{\partial\tilde{u}_i}{\partial x_k}\right)$$

$$D_{ij} = -\left(\bar{\rho}\,\widetilde{u_i''u_k''}\frac{\partial\tilde{u}_k}{\partial x_j} + \bar{\rho}\,\widetilde{u_j''u_k''}\frac{\partial\tilde{u}_k}{\partial x_i}\right)$$

$$c_1 = 3.2f_AA_2^{\frac{1}{2}}\min\left[(Re_t/160)^2, 1\right], \qquad c_1' = 1.1$$

$$c_2 = \min\left\{0.55\left[1 - \exp\left(-A^{\frac{3}{2}}Re_t/100\right)\right], 3.2A/(1+S)\right\}$$

$$c_2' = \min\left[0.6, A^{\frac{1}{2}}\right] + 3.5(S-\Omega)/(3+S+\Omega) - 4\min[S_I, 0]$$

$$S = \frac{\tilde{k}}{\tilde{\epsilon}}\sqrt{\frac{1}{2}S_{ij}S_{ij}}, \qquad \Omega = \frac{\tilde{k}}{\tilde{\epsilon}}\sqrt{\frac{1}{2}\Omega_{ij}\Omega_{ij}}$$

$$S_I = \sqrt{6}S_{ij}S_{jk}S_{ki}/(S_{ln}S_{ln})^{\frac{3}{2}}$$

$$S_{ij} = \frac{\partial\tilde{u}_i}{\partial x_j} + \frac{\partial\tilde{u}_j}{\partial x_i}, \qquad \Omega_{ij} = \frac{\partial\tilde{u}_i}{\partial x_j} - \frac{\partial\tilde{u}_j}{\partial x_i}$$

$$f_{w1} = 2.35\left(1 - A^{\frac{1}{2}}\right)\min[1, \max(0, 1 - (Re_t - 55)/70)]$$

$$f_{w2} = 0.6A_2\left(1 - A^{\frac{1}{2}}\right)\min[1, \max(0, 1 - (Re_t - 50)/85)] + 0.1$$

$$f_I = 3f_A, \qquad f_A = \begin{cases} (A/14)^{\frac{1}{2}} & A < 0.05 \\ A/0.7^{\frac{1}{2}} & 0.05 < A < 0.7 \\ A^{\frac{1}{2}} & A > 0.7 \end{cases}$$

The scaling of f_{w1} and f_{w2} by $(1 - A^{\frac{1}{2}})$ and their functional dependence on Re_t ensures that the inhomogeneity corrections are effective only near walls, the target area being the region $Re_t < 100$.

The invariant S_I takes the values $+1$ or -1 in homogeneous axisymmetric contraction or expansion, respectively, but vanishes in plane strain. It is used here to modify the c_2' coefficient to improve the representation of axisymmetric-expansion flow, which is also a key feature of the impinging jet discussed in Sec. IV.C.

D. Dissipation Tensor: ε_{ij}

The dissipation tensor is formulated using a blend of isotropic and wall-limiting (ϵ_{ij}') values, with an additional proposal (ϵ_{ij}''), due to Craft and Launder,[17] to account for the dip in the shear-stress dissipation rate in the buffer layer:

$$\epsilon_{ij} = (1 - f_\epsilon)\bar{\rho}(\epsilon_{ij}' + \epsilon_{ij}'')/D + \tfrac{2}{3}f_\epsilon\bar{\rho}\tilde{\epsilon}\delta_{ij} \quad (7)$$

with

$$\epsilon_{ij}' = \tilde{\epsilon}\frac{\widetilde{u_i''u_j''}}{\tilde{k}} + 2\tilde{\nu}\frac{\widetilde{u_l''u_n''}}{\tilde{k}}\frac{\partial\sqrt{\tilde{k}}}{\partial x_l}\frac{\partial\sqrt{\tilde{k}}}{\partial x_n}\delta_{ij}$$
$$+ 2\tilde{\nu}\left(\frac{\widetilde{u_l''u_i''}}{\tilde{k}}\frac{\partial\sqrt{\tilde{k}}}{\partial x_j}\frac{\partial\sqrt{\tilde{k}}}{\partial x_l} + \frac{\widetilde{u_l''u_j''}}{\tilde{k}}\frac{\partial\sqrt{\tilde{k}}}{\partial x_i}\frac{\partial\sqrt{\tilde{k}}}{\partial x_l}\right)$$

$$\epsilon_{ij}'' = f_R\tilde{\epsilon}\left[2\frac{\widetilde{u_l''u_k''}}{\tilde{k}}d_l^Ad_k^A\delta_{ij} - \frac{\widetilde{u_l''u_i''}}{\tilde{k}}d_l^Ad_j^A - \frac{\widetilde{u_l''u_j''}}{\tilde{k}}d_l^Ad_i^A\right]$$

$$D = \frac{\epsilon'_{ij} + \epsilon''_{ij}}{2\tilde{\epsilon}}$$

$$f_R = (1 - A)\min[(Re_t/80)^2, 1], \qquad f_\epsilon = A^{\frac{1}{2}}$$

E. Dissipation-Rate Equation

An equation for the homogeneous dissipation rate $\tilde{\epsilon}^*$ is proposed, which uses conventional $C_{\epsilon 1}$ and $C_{\epsilon 2}$ constants, but incorporates a modified form of the length-scale moderator developed by Iacovides and Raissee[24] (itself developed from an original proposal of Jakirlić and Hanjalić[25]). The form currently adopted is

$$\frac{\partial \bar{\rho}\tilde{\epsilon}^*}{\partial t} + \frac{\partial \bar{\rho}\tilde{\epsilon}^*\tilde{u}_k}{\partial x_k} = \frac{\partial}{\partial x_l}\left[\left(\tilde{\mu}\,\delta_{lk} + C_\epsilon \bar{\rho}\widetilde{u''_l u''_k}\frac{\tilde{k}}{\tilde{\epsilon}}\right)\frac{\partial \tilde{\epsilon}^*}{\partial x_k}\right] + \frac{C_{\epsilon 1}\bar{\rho}P_k}{\tau} - \frac{C_{\epsilon 2}\bar{\rho}\tilde{\epsilon}^*}{\tau} - \frac{C_{\epsilon 3}(\tilde{\epsilon} - \tilde{\epsilon}^*)\bar{\rho}\tilde{\epsilon}^*}{\tilde{k}} + C_{\epsilon 4}\tilde{\mu}\,\tau\widetilde{u''_i u''_j}\frac{\partial^2 \tilde{u}_k}{\partial x_i \partial x_l}\frac{\partial^2 \tilde{u}_k}{\partial x_j \partial x_l} + \frac{C_{\epsilon 5}\bar{\rho}\tilde{\epsilon}^*}{\tau}Y_P \tag{8}$$

where

$$Y_P = 0.2\min\{\max[F(F+1)^2, 0], 20\}$$

$$F = \left[\sqrt{\left(\frac{\partial l}{\partial x_j}\right)\left(\frac{\partial l}{\partial x_j}\right)} - \frac{\partial l_e}{\partial Y}\right]\Big/ c_l$$

$$\frac{\partial l_e}{\partial Y} = c_l[1 - \exp(-B_\epsilon Re_t) + B_\epsilon Re_t \exp(-B_\epsilon Re_t)]$$

$$c_l = 2.55, \qquad B_\epsilon = 0.1069, \qquad \tau = \frac{\tilde{k}}{\tilde{\epsilon}}$$
$$C_{\epsilon 1} = 1.44, \qquad C_{\epsilon 2} = 1.92, \qquad C_{\epsilon 3} = 1.0$$
$$C_{\epsilon 4} = 0.4, \qquad C_{\epsilon 5} = 0.2, \qquad C_\epsilon = 0.18$$

F. Turbulent Heat Fluxes

To avoid additional transport equations for the velocity–temperature correlations, $\widetilde{T''u''_i}$, appearing in the mean total-energy equation, a common modeling practice is to employ the GGDH:

$$-\bar{\rho}\widetilde{T''u''_i} = c_\theta \frac{\bar{\rho}\tilde{k}}{\tilde{\epsilon}}\widetilde{u''_i u''_k}\frac{\partial \tilde{T}}{\partial \tilde{x}_k} \tag{9}$$

with, typically, $c_\theta = 0.3$. This approach has occasionally been found to be numerically destabilizing in regions where the GGDH implies a high countergradient temperature transport. Although this may partly be attributed to the nature of the present implicit numerical solver, a block line-relaxation procedure requiring a diagonally dominant matrix for convergence, other physical and numerical features also play a role. Thus, for certain test cases (not documented here) involving large temperature gradients in conjunction with highly skewed near-wall cells, it proved impossible to stabilize calculations using the specified GGDH for any size of time step. Furthermore, because of the very large cell-aspect ratios in the near-wall region, it is usually not possible to resolve the wall-parallel heat-flux gradients with any degree of accuracy. In the present work, the turbulent heat fluxes are, therefore, determined from a thin-layer form of Eq. (9). By noting that the required numerical flux is that component of the heat flux resolved in the direction $\boldsymbol{n}$ normal to the cell face, we obtain this directly as

$$-\bar{\rho}\widetilde{T''u''_i}n_i = c_\theta \frac{\bar{\rho}\tilde{k}}{\tilde{\epsilon}}\widetilde{u''_i u''_k}n_i n_k n_j \frac{\partial \tilde{T}}{\partial \tilde{x}_j} \tag{10}$$

Although the modified, thin-layer heat-flux model (10) is not strictly frame invariant, it provides an anisotropic face diffusivity that is nonnegative, provided that the Reynolds stresses satisfy a strong realizability condition, namely, nonnegative normal stresses and a Schwartz-type inequality on the shear stresses.

III. Numerical Implementation

The model has been implemented within the implicit Riemann-solver-based numerical framework developed by Batten et al.[26] Mean-flow and turbulence quantities are solved simultaneously, but the block structure is simplified using a Patankar-type linearization for all turbulence-model variables, as described in Ref. 26. To help stabilize the Reynolds-stress computations at large Courant–Friedrichs–Lewy (CFL) numbers and high turbulence intensities, a block-coupled extension of the apparent viscosity technique developed by Huang and Leschziner[27] is included in the mean-flow Jacobians. The cell-face values of the traction vectors appearing in the mean-flow equations, $t_i = \widetilde{u''_i u''_j}n_j$, are currently determined by linear interpolation from adjacent cell centers, although work is in progress toward a strongly coupled technique in which the traction vectors and the anisotropic pressures are combined in a single wave model.[28] For flows involving shock waves, the CFL number is typically raised from 1 to 10^3 at a rate of about 1.1 per time step.

Axisymmetric flows have been computed by solving the full three-dimensional system of equations on a mesh generated by rotating a two-dimensional cardinal grid through a small angle, $\pm\theta$, with symmetry conditions imposed on the segment faces.

IV. Results

A rational sequence of test cases has been computed to show the predictive performance of the present Reynolds-stress model relative to other models across a broad range of conditions. The choice of cases was motivated by the desire to demonstrate performance for simple flows, generally regarded as key calibration cases, before presenting results for compressible flows. The inclusion of the first group is especially important if, as is the case here, an existing model has been substantially modified to achieve improved performance for a particular flow category.

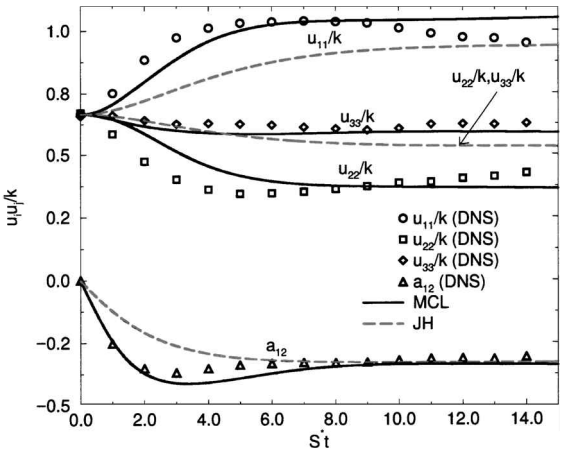

Shear

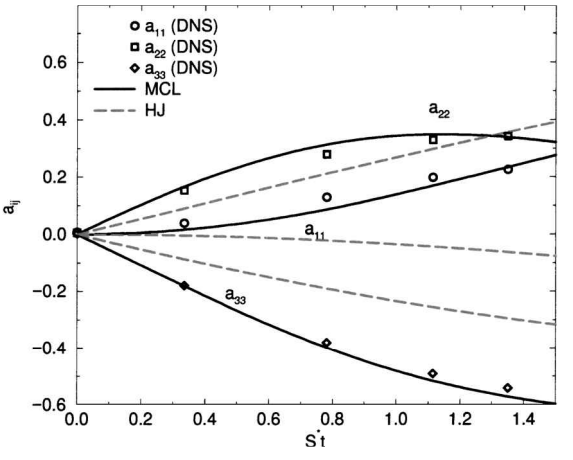

Plane strain

Fig. 2 Homogeneous shear and plane strain.

In the discussion to follow, the modified version of the Craft–Launder model (MCL) is compared with the Launder–Sharma[20] linear k–ϵ model (k–ϵ), Menter's shear-stress-transportmodel[1] (SST), and the Jakirlić–Hanjalić Reynolds-stress model (JH).[25] Depending on the flow considered, certain comparisons are made against either the k–ϵ model or Menter's SST model,[1] as representatives of the linear eddy-viscosity framework. This selective approach to the lowest-order background model is motivated by the wish to convey a fair picture of its capabilities, taking into consideration the generally poor performance of the conventional k–ϵ model in separated flow (see, e.g., Refs. 1 and 29).

A. Homogeneous Flows

The first set of tests focuses on homogeneous turbulence induced and sustained by irrotational straining. Four cases are considered: simple shear, compared with DNS data by Matsumoto et al.,[30] and plane strain, axisymmetric contraction, and axisymmetric expansion, compared with DNS data by Lee and Reynolds.[31] The stress components are plotted against $t' = S^* t$, where $S^* = (k/\epsilon)\sqrt{(S_{ij}S_{ij}/2)}$ is the mean-strain-rate parameter and t is time. Figures 2 and 3 also show comparisons against the JH model,[25] which uses the isotropization of production (IP) pressure–strain model of Naot et al.[32] As seen, the IP model displays the wrong trend for a_{11} in the plane-strain case and fails to separate anisotropy components whose corresponding stresses have no production source. The present cubic model displays reasonably good agreement throughout.

B. Plane Channel Flow

A fully developed, plane-symmetric channel flow at $Re_\tau = 180$ has been computed using the original Craft–Launder model[17] (CL), the current modified variant (MCL) and the JH model.[25] The results

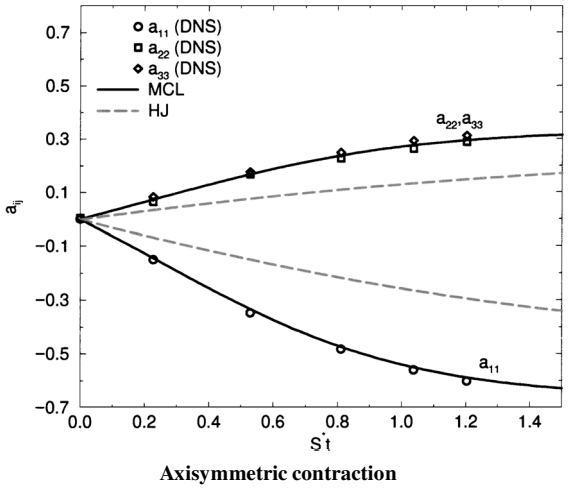

Axisymmetric contraction

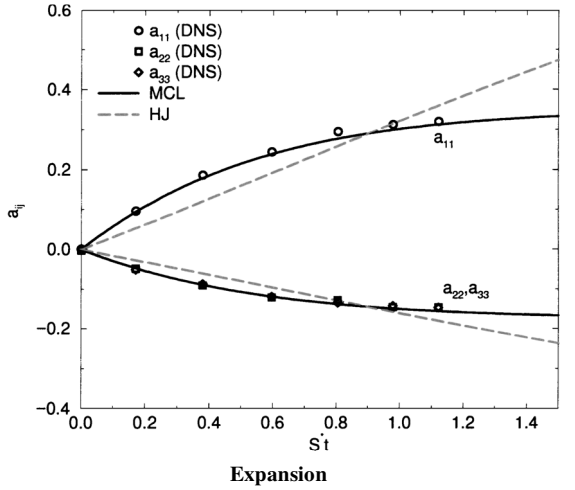

Expansion

Fig. 3 Homogeneous axisymmetric contraction and expansion.

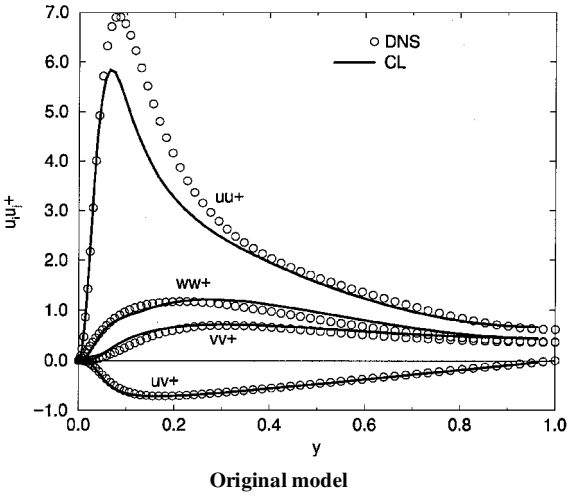

Original model

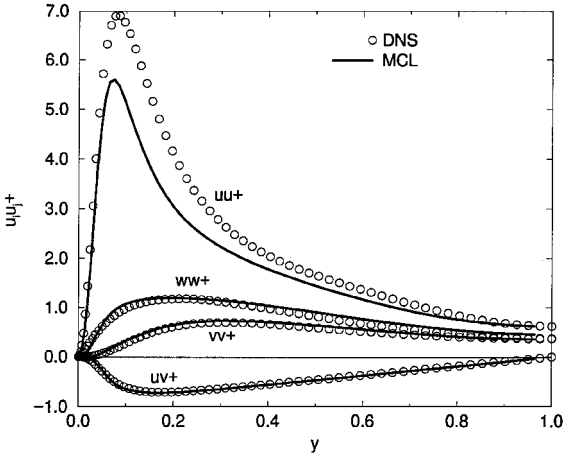

MCL

Fig. 4 Channel flow at $Re_\tau = 180$.

are compared in Figs. 4 and 5 against the DNS data of Kim et al.[33] Predictions were obtained with a nonuniform mesh of 50 points, which is known to support grid-independent solutions for all quantities, with the wall-nearest node located at a distance corresponding to $y^+ \approx 0.5$.

The results are generally in good agreement with DNS, with all models returning a strong separation between the normal stresses. Although there is a tendency for all variants to underpredict the near wall $\widetilde{u_1''u_1''}$, this defect is of no direct consequence in this particular flow, as the shear stress is principally sensitive to the wall-normal intensity.

C. Impinging Jet Flow

This incompressible flow consists of a round air jet discharging from a smooth pipe and then impinging normally on a flat plate. Mean-flow and turbulence measurements were performed by Cooper et al.,[34] and these have been used extensively for benchmarking turbulence models. The particular case considered here is at a discharge height, $H = 2D$, and $Re = 2.3 \times 10^4$, based on bulk velocity and internal pipe diameter D. The jet-exit conditions were first determined from a fully developed pipe flow calculation. A 121×121 grid was then used, with $y^+ < 0.5$ on both plate and pipe walls and with 51 points across the jet radius. Grid independence was confirmed with a finer 180×180 mesh using a similar spacing for the wall-nearest nodes. Reservoir conditions, corresponding to constant stagnation temperature and pressure, were imposed on the upper entrainment boundary outside the pipe. The outflow boundary extended 8 jet diameters from the pipe centerline. Figures 6–12 present profiles of mean velocity and turbulent stresses, the distribution of Nusselt number at the impingement plate, and the convergence histories for the four models identified earlier.

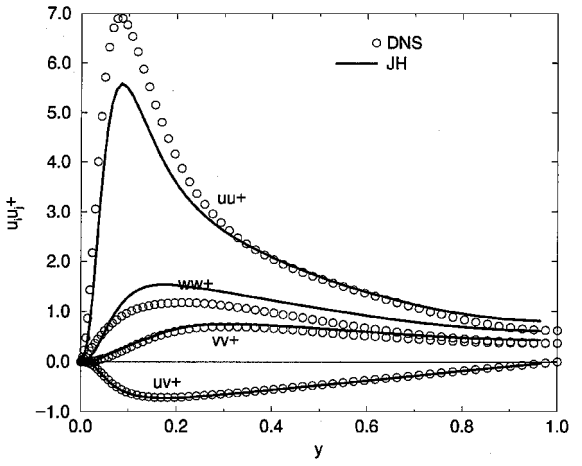

JH model

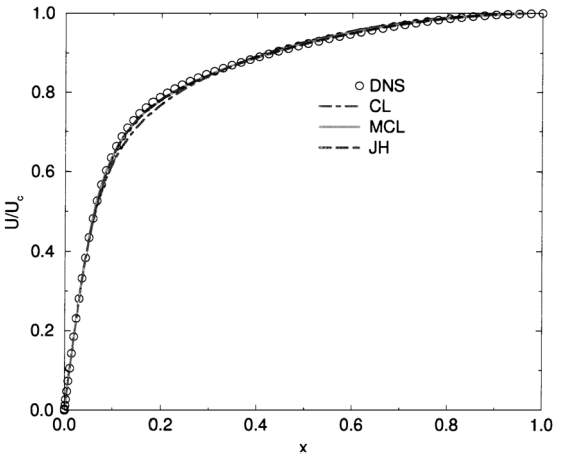

Mean-velocity predictions

Fig. 5 Channel flow at $Re_\tau = 180$.

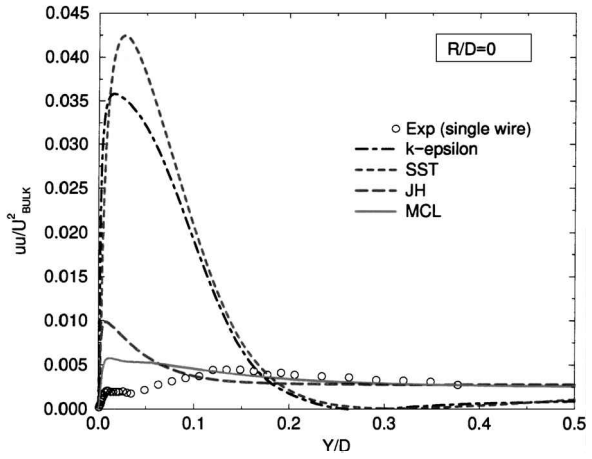

Fig. 6 Impinging jet: axial normal stresses on stagnation line.

Two especially challenging features of this flow are the highly curved outer shear layer of the jet and the region of strong irrotational straining associated with impingement. Linear eddy-viscosity models are known to reflect poorly the response of turbulence to both curvature and normal straining. The most noticeable defects of the linear k–ϵ and SST models occur in the stagnation region, which is characterized by high rates of normal straining, and where both models show a massive overprediction of k and thus of all normal stresses (Fig. 6). The SST model is worse than the k–ϵ model on the stagnation line, but recovers later once the flow turns and the turbulent boundary layer on the plate starts to develop. The JH model[25] gives only a modest improvement over the k–ϵ model. This is due, in part, to weaknesses with the conventional wall-reflection terms

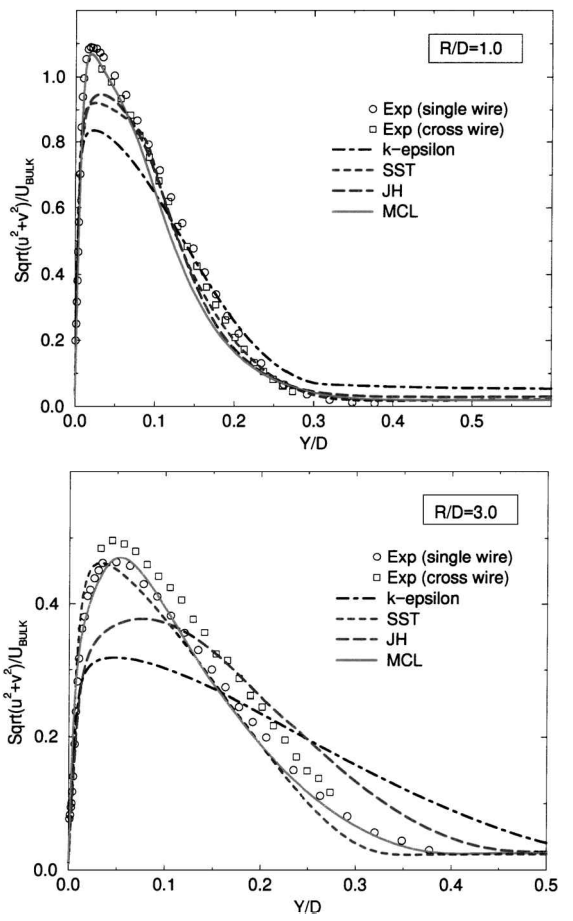

Fig. 7 Impinging jet: mean-velocity profiles at $R/D = 1$ and 3.

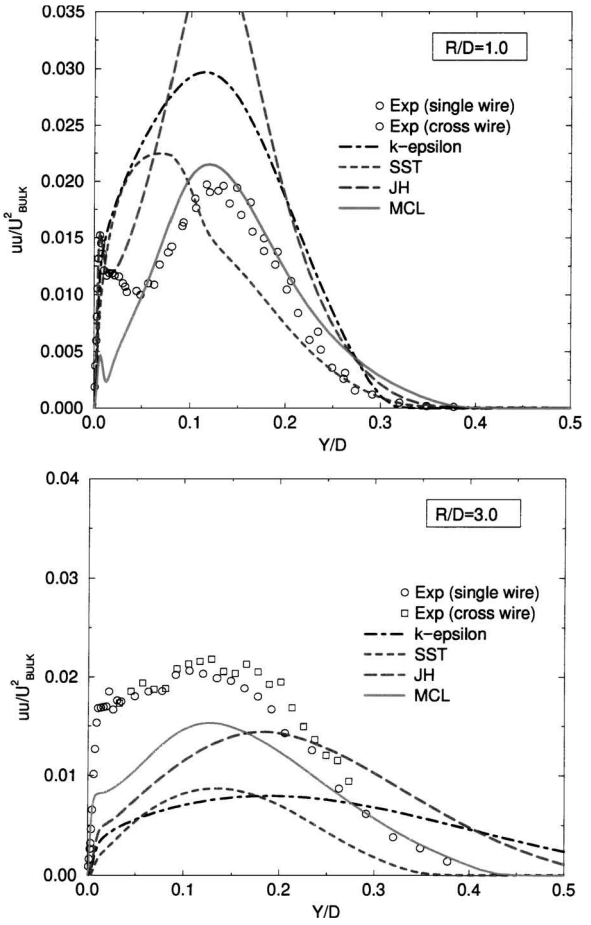

Fig. 8 Impinging jet: radial normal stresses at $R/D = 1$ and 3.

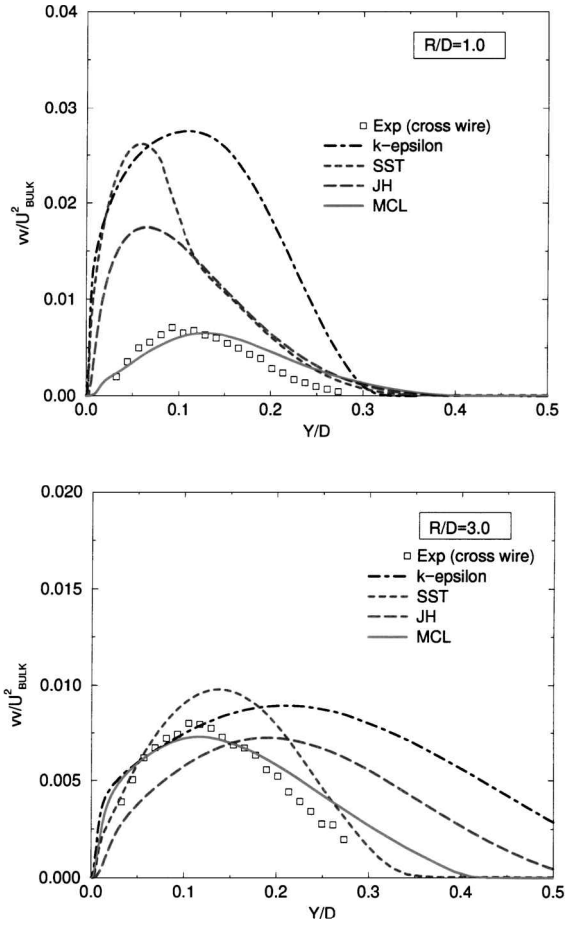

Fig. 9 Impinging jet: axial normal stresses at $R/D = 1$ and 3.

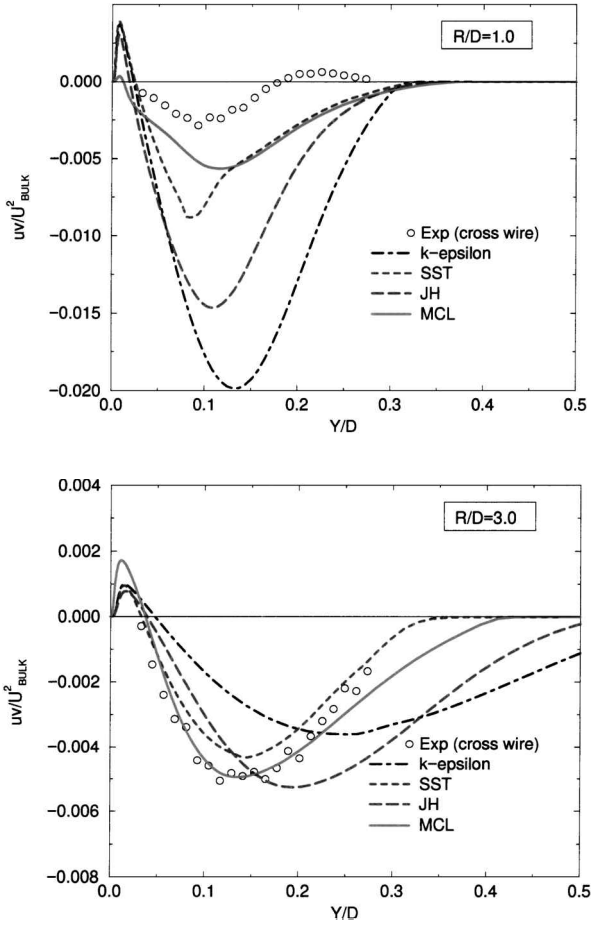

Fig. 10 Impinging jet: shear stresses at $R/D = 1$ and 3.

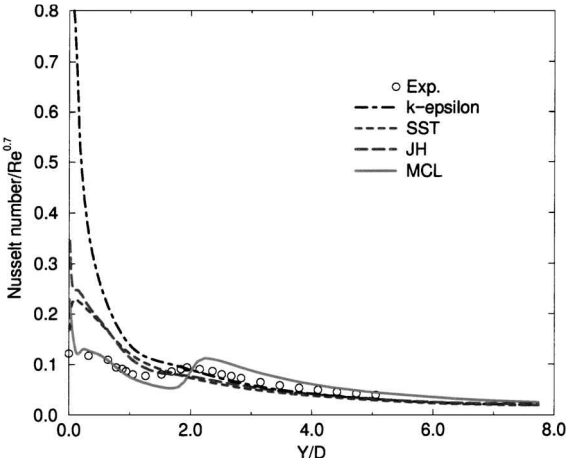

Fig. 11 Impinging jet: heat transfer.

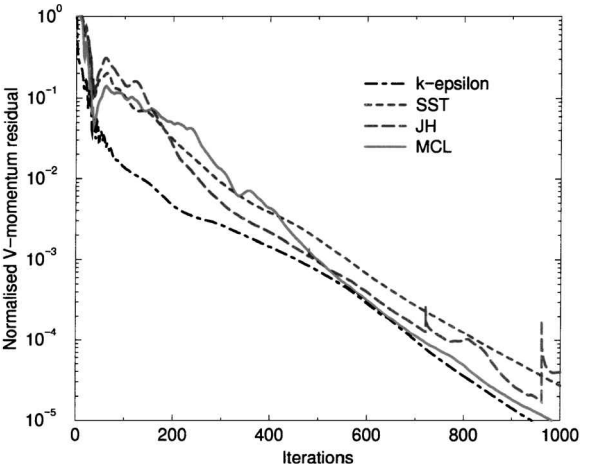

Fig. 12 Impinging jet: convergence.

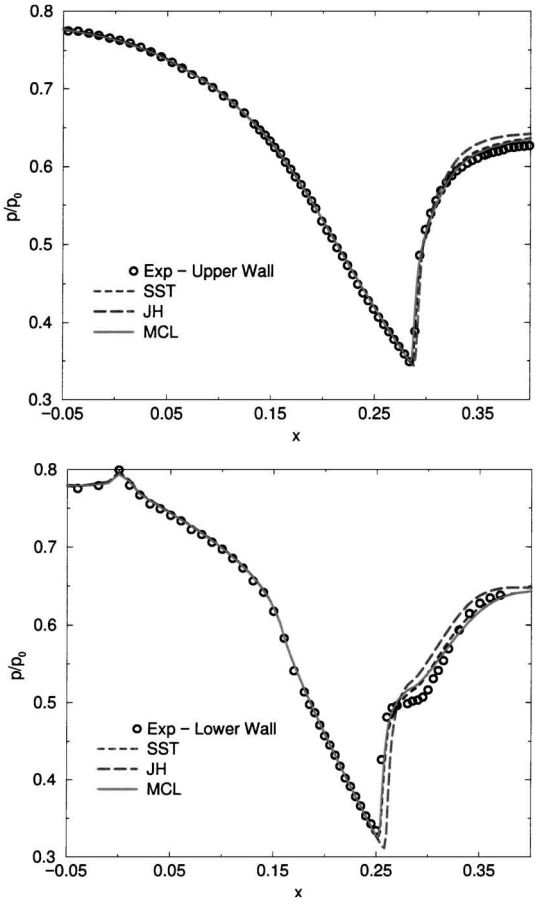

Fig. 13 Délery's case C: wall-pressure distributions.

used in this model (see, e.g., Ref. 35). The predictions of the MCL model are generally good, although the small secondary peaks in the near-wall radial normal stress are still not well captured, perhaps due to defects in the predicted near-wall turbulence length scale to which the near-wall stresses are sensitive. The heat-transfer predictions, shown in Fig. 11, are, of course, extremely sensitive to the turbulence level in the viscous sublayer and, hence, to subtle details of the near-wall modeling and numerical implementation. Clearly, the relationship between the turbulence level and heat transfer is reflected by the solutions obtained with the k–ϵ and Reynolds-stress models. Curiously, however, the SST model does not conform to this expected dependence, and this suggests that the near-wall behavior of ω, the turbulence vorticity representing the turbulent length scale, is of crucial importance to the depression of the Nusselt number, particularly in the impingement region. Convergence histories are shown in Fig. 12, in terms of the normalized sum of the absolute momentum residuals, and these demonstrate that all models converge satisfactorily at a similar rate. The solutions experience no change below a convergence level of 10^{-3}.

D. Transonic Flow over a Plane Channel Bump: Délery's Case C

This well-known, nominally two-dimensional, transonic-flow test case has featured in several past collaborative validation projects and workshops as a benchmark for turbulence models in shock-wave/boundary-layer interaction flows.[36–38] The geometry consists of a channel with a slightly sloping upper wall and a bump on the lower wall, representative of the suction side of a transonic-wing profile. Known upstream reservoir conditions of 300 K and 96 kPa were prescribed at the domain inlet. Downstream, there is a second, adjustable throat, which can be used to vary the mass-flow rate and, hence, the location of the shock downstream of the first throat. In the experiment, the back pressure is adjusted until a shock forms at the desired location. This is mimicked in the present computations by adjusting the back pressure to match the location of the upper-wall shock, with differences in the turbulence models necessitating slightly different back pressures in each case. The MCL and SST models used $p_{\text{exit}} = 61$ kPa, whereas the k–ϵ and JH models used $p_{\text{exit}} = 61.5$ kPa.

A 121×121 nonuniform grid was used. Streamwise clustering in the shock-interaction region and normal-to-wall clustering ensured that $y^+ < 0.5$ everywhere. This grid was selected after grid-independence tests with up to 221×221 nodes. The upper and lower walls of the channel were assumed adiabatic.

Wall-pressure distributions are compared to experimental data in Fig. 1 for the k–ϵ and original CL models[17] and in Fig. 13 for the SST, JH, and the current MCL variant. Figure 14 compares predicted

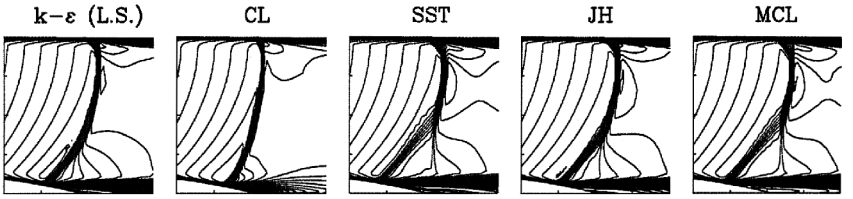

Fig. 14 Délery's case C: iso-Mach contours in interaction region.

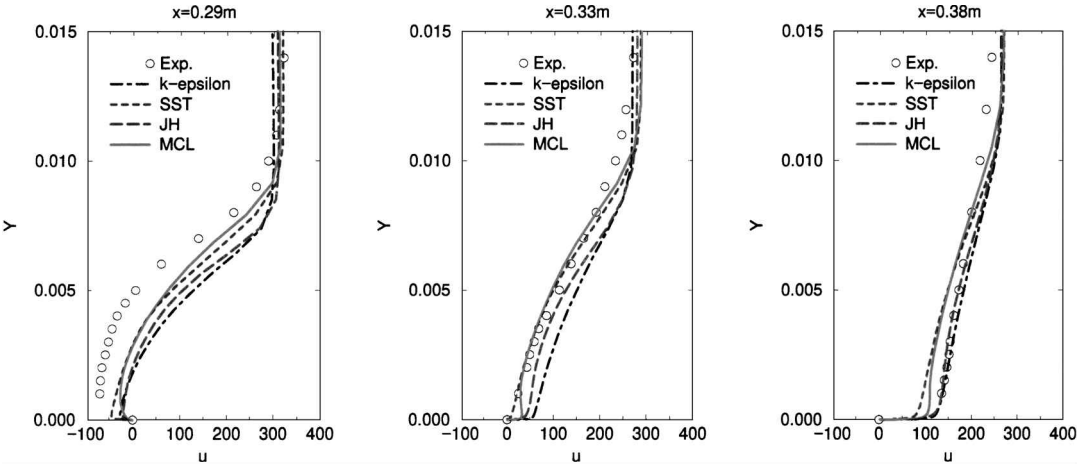

Fig. 15 Délery's case C: streamwise mean-velocity distributions.

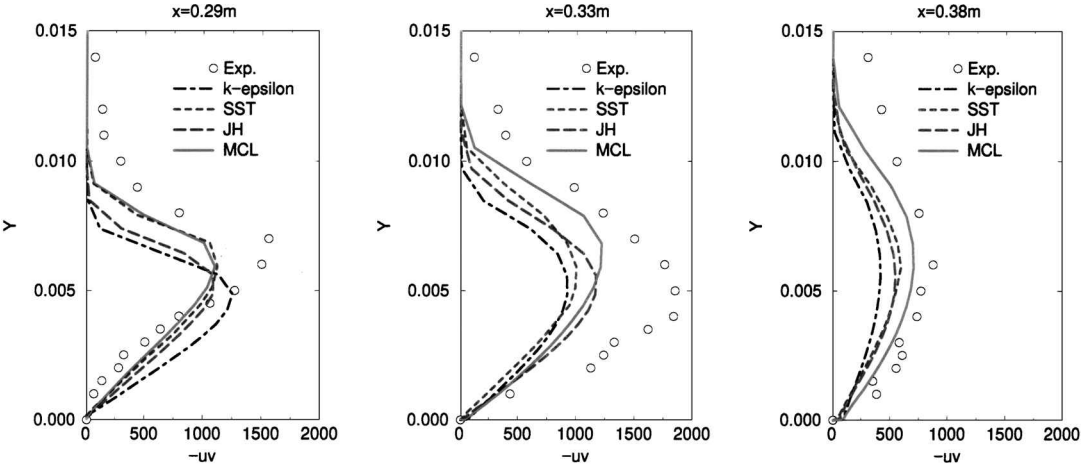

Fig. 16 Délery's case C: shear-stress distributions.

iso-Mach contours for the five models. For reasons discussed in the Introduction, the CL model gives wholly unrealistic predictions downstream of the shock wave, resulting in poor wall-pressure distributions and the absence of the expected lambda-shock structure. For this test case, the normal stresses do not contribute significantly to the mean-flow behavior, and as a result, the well-predicted shear stress obtained with the SST model gives a mean-flow solution that is comparable with the present Reynolds-stress closure.

Figures 15 and 16 show profiles of velocity and shear stresses, respectively, at locations $x = 290$, 330, and 380 mm. The JH model gives the least significant improvement over the k–ϵ solution, with both mean flow and shear stresses indicating an underestimation of the extent of the shock-induced separation.

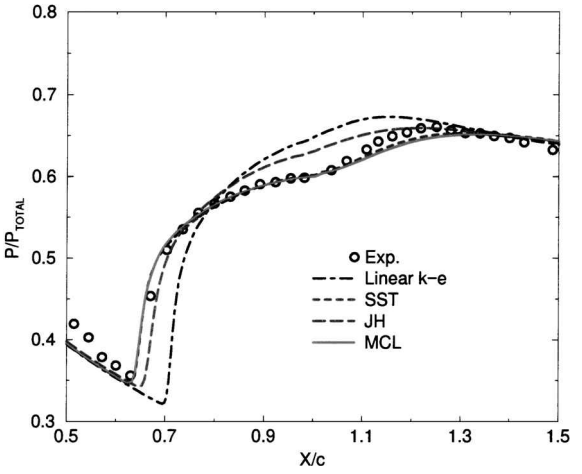

Fig. 17 Bachalo and Johnson[40] bump: wall-pressure distributions.

E. Transonic Flow over an Axisymmetric Bump

This case, examined experimentally by Johnson et al.[39] and Bachalo and Johnson,[40] is the axisymmetric equivalent of the preceding flow and has also been used extensively for model benchmarking. It distinguishes itself by the absence of distortions arising from three-dimensional features, which pose some uncertainties in the earlier flow. The geometry consists of a cylinder, with a circular-arc bump of 20.3-cm chord. The freestream Mach number is $M = 0.875$, and the total pressure and temperature are 95 kPa and 302 K, respectively.

A 180×110 grid was used, with clustering applied around the shock and near the wall, the latter to ensure $y^+ < 0.5$ everywhere. This resolution was found to support grid-independent solutions using the present numerical scheme. At the inlet, the velocity was assumed to be parallel to the cylinder axis, and a 4-mm-thick boundary layer was imposed, using a compressible Musker formulation. The wall was assumed to be isothermal, and the freestream static pressure was imposed at the subsonic exit of the domain.

Figures 17–19 give comparisons for wall pressure, velocity, and shear stress, respectively, predicted by the k–ϵ, SST, JH, and MCL models. The present MCL model is seen to return a considerably more pronounced pressure-plateau region than do the k–ϵ and JH models, predicting a shock location that is fractionally too far upstream. Here again, the SST model gives a performance very similar to the present model, for reasons discussed in the preceding section. As for velocity and shear-stress profiles, the present model and the

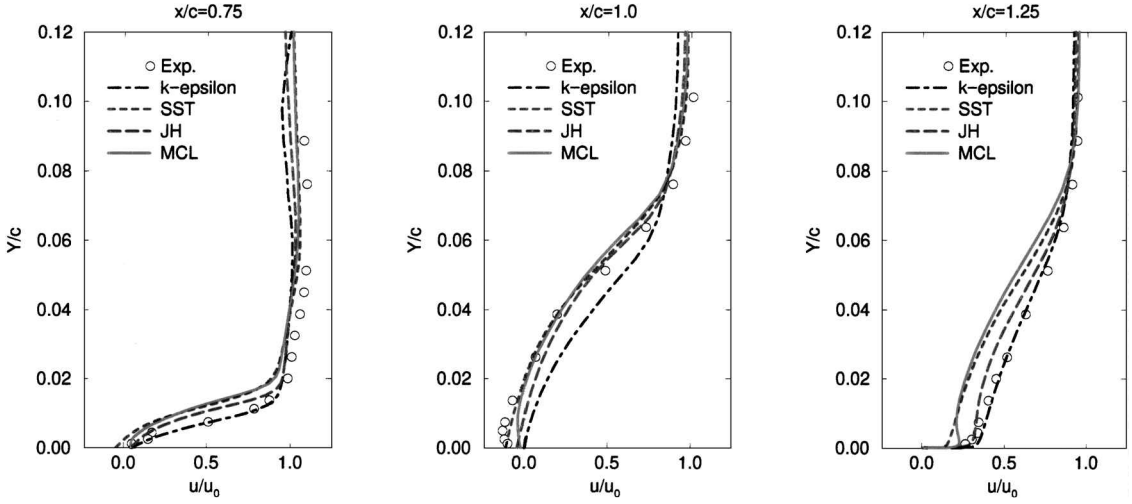

Fig. 18 Bachalo and Johnson[40] bump: velocity profiles.

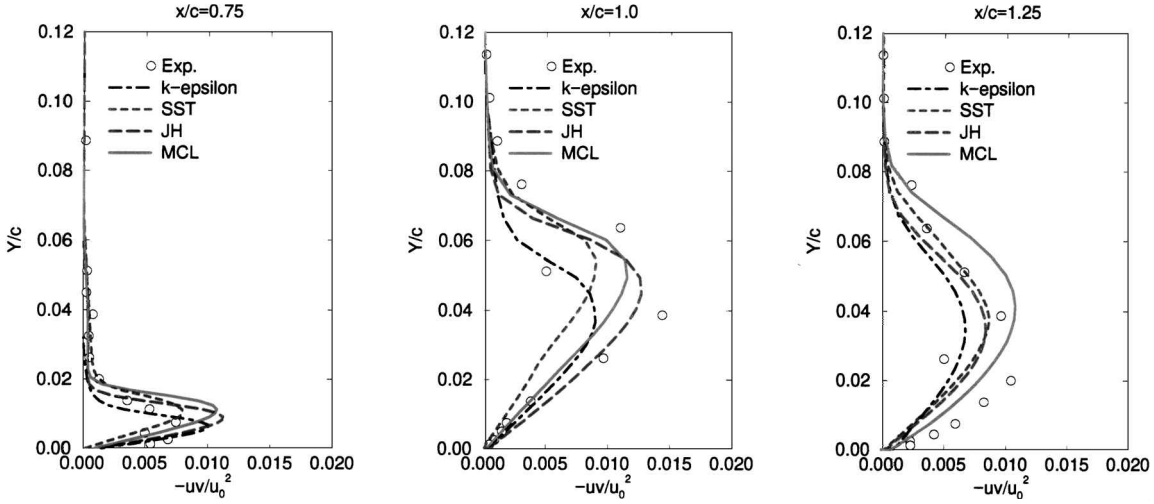

Fig. 19 Bachalo and Johnson[40] bump: shear-stress profiles.